Component-dependent lattice distortions and atomic scale insights in multi-component Au-Cu-Ni-Pd-Pt based alloys

Sophie Drescher [1,2 ✉], Alexei Kuzmin [3 ✉], Edmund Welter[4], Jens Freudenberger[1,2], and Alevtina Smekhova [5 ✉]

[1] Leibniz Institute for Solid State and Materials Research, D-01069 Dresden, Germany
[2] TU Bergakademie Freiberg, Institute of Materials Science, D-09599 Freiberg, Germany
[3] Institute of Solid State Physics, University of Latvia, LV-1063 Riga, Latvia
[4] Deutsches Elektronen-Synchrotron (DESY), A Research Centre of the Helmholtz Association, D-22607 Hamburg, Germany
[5] Helmholtz-Zentrum Berlin für Materialien und Energie (HZB), D-12489 Berlin, Germany

ABSTRACT: In our study, the composition-dependent effects of atomic displacements in Au-Cu-Ni-Pd-Pt based alloys, comprising elements with large differences in atomic radii, are investigated at the atomic scale. Two alloys—the equimolar AuCuNiPdPt and AuCuNiPd—have been characterized using multi-edge extended X-ray absorption fine structure (EXAFS) spectroscopy in conjunction with reverse Monte Carlo (RMC) simulations at room temperature. The statistically-averaged component-dependent pair distribution functions (PDFs), which represent the distribution of atoms around the assumed regular face-centered cubic (fcc) lattice positions, reveal a shift of their peaks to shorter distances and a pronounced asymmetry in atomic distribution only for atoms with small radii (Cu/Ni). The analysis demonstrates that small atoms (Cu/Ni) are significantly more displaced from the expected lattice positions as compared to large atoms (Au/Pt). Furthermore, there are indications of preferential next-neighbour bonding that changes depending on the alloy composition. The most pronounced changes in the PDFs were found solely for Pd. With this study, we provide a basis for a deeper understanding of the composition-dependent atomic arrangement in chemically complex solid solutions.

KEYWORDS: high-entropy alloys, short-range order, solid solution strengthening, extended X-ray absorption fine structure (EXAFS) spectroscopy, reverse Monte Carlo

1 Introduction

The alloying of different elements for improving particular macroscopic properties of metals has been known since ancient times. Starting from only two elements commonly available in the Bronze Age, it was nowadays developed into complex and precise technology for accurate mixing of many more components in a broad range of desired proportions. The chemical complexity of multi-principal-component alloys achieved during such a process results in a variety of attractive properties connected to the compositional disorder through many different local atomic environments and interactions. At the same time, it raises a question of whether common approaches previously used to describe conventional alloys with a depicted base element are also suitable for a new class of compositionally complex systems as high-entropy alloys (HEAs), which are recognised by a near-equimolar mixing of five or more principal components without unique base element.

As a general rule, it is widely accepted that alloying of different-sized elements taking place in ordinary alloys leads to noticeable lattice distortions, i.e., to pronounced displacements of individual elements from their equilibrium positions in the ideal lattice. It is also stated that lattice distortions are more severe in HEAs than in conventional alloys, even without quantifying what "severe" means. There is already strong evidence that lattice distortions can be associated with several peculiar HEA properties, such as enhanced solid solution strengthening (SSS) [1−4], high wear resistance [5, 6], high catalytic activity [7, 8], low thermal conductivity, i.e., good thermoelectric performance [9, 10], and good irradiation resistance [11−13]. Moreover, due to the almost unlimited compositional space formed by this particular class of alloys, many further exceptional property combinations can be expected.

✉Address correspondence to Sophie Drescher, sophie.drescher @doktorand.tu-freiberg.de; Alexei Kuzmin, a.kuzmin@cfi.lu.lv; Alevtina Smekhova, alevtina.smekhova@helmholtz-berlin.de

Additionally, lattice distortions play a crucial role in the mechanical properties of multi-principal element alloys including HEAs, significantly influencing dislocation mobility for both edge and screw dislocations [3, 14]. These distortions impact the core structure of edge dislocations, leading to increased critical shear stresses for dislocation motion [15], and contribute to strain hardening [16]. Understanding these effects is crucial for predicting and optimizing the mechanical properties of multi-principal element alloys, including plasticity, dislocation activity, and strength. It has already been reported that the degree of lattice distortions depends on the constituent elements and their concentrations, reaching maximum values at equiatomic compositions [15]. Nutor et al. [17] emphasized that severe lattice distortions are a key factor in determining the properties of HEAs, including their mechanical properties and the ability to overcome the strength–ductility trade-off.

Another consequence of alloying is its implications on the Goldschmidt radius, which is commonly determined for each element upon the next neighbour distance assuming the hard-sphere model [18]. Despite the size of the element is influenced by the character of bonding, like metallic vs. covalent, and may change during the alloying process, the Goldschmidt radii for the given element are assumed to not severely differ in mutual surroundings. So, the radii of the individual elements are often regarded as a fixed value for alloys (including HEAs) even if they can differ from the radii of pure elements.

A significant part of research in the field of different HEAs is currently focused on a better understanding of the underlying mechanisms of their strength behavior. One of the key problems is the theoretical modeling of SSS with an overall goal to develop a theory for promising HEAs predictions in a vast compositional space [4]. The searching approach in this direction includes a better understanding of the role of lattice distortions in chemically complex alloys first, and only later their correlations with the strength behavior. Commonly, establishing a relation between macroscopic properties and the lattice distortions is done with the use of term, given by the concentration-weighted average of the elemental radii differences [19]. On the contrary, the model of Varvenne [20] approximates the stress–strain fluctuations via the concentration-weighted (x_i) average of the misfit volumes (ΔV_i) normalized on the Burgers vector (b) as $\delta = \left(\sum_i x_i \Delta V_i^2 / 9b^6 \right)^{0.5}$, with further use of this quantity as a key parameter for the description of SSS in terms of elastic solute–dislocation interactions. However, the δ parameter provides only a single value for an entire alloy and implies that the variations of the local bond distances or atomic volumes are directly correlated with the misfit strains, which does not necessarily have to be the case [4]. The existing theoretical models can nevertheless be validated in the experiment with exclusively single-phase HEAs and preferentially over a large compositional space. In this regard, the HEA system based on Au-Cu-Ni-Pd-Pt [21] is very attractive since its single-phase state remains unchanged within a wide range of composition variations, as proven in Refs. [22–24].

Understanding and advanced structural characterization of lattice distortions in HEAs are challenging tasks that up to now were only rarely addressed experimentally: Little is known about the influence of a particular principal component on the positional disorder in compositionally complex systems due to, e.g., a change in binding characteristics. This leads to a very complex picture where an energy landscape determines the stiffness, chemical potential, equilibrium distance, and atomic sizes that are not independent of each other, and all together influence the component-dependent local lattice relaxations (see, e.g., Refs. [17, 25–28]).

A possibility to access the δ parameter experimentally was proposed by Okamoto et al. [29], who suggested determining the mean atomic displacement using single crystal X-ray diffraction (XRD) and density functional theory (DFT) calculations. As it was demonstrated in the case of Cantor alloy and its derivates, the square root of the average mean square atomic displacement is directly correlated with the yield strength normalized by the shear modulus, showing that the strength in Cr-Mn-Fe-Co-Ni is dominated by elastic interactions [29]. The Au-Cu-Ni-Pd-Pt system has much stronger differences in the atomic sizes of principal components as compared to the Cantor alloy based on 3d elements Cr, Mn, Fe, Co, and Ni, thus, triggering an excessive interest in the investigation of the component-dependent local lattice distortions and their correlations with the macroscopic properties. In particular, the correlation between lattice distortions and unexpectedly high yield strength of 880 MPa found for the single-phase face-centered cubic (fcc) equiatomic AuCuNiPdPt alloy [30] is greatly intriguing. As the elastic interactions are supposed to be correlated by the mean atomic displacement of the atoms from their ideal positions [29], a deviation of these correlations may impact the SSS underlying mechanisms. In this way, it can be clarified whether the strength in Au-Cu-Ni-Pd-Pt alloys is mainly determined by elastic interactions or whether other interactions require consideration as well.

As was shown for binary AuNi and AuCu systems by extended X-ray absorption fine structure (EXAFS) spectroscopy, the interatomic distances between non-equivalent constituents with large differences in the atomic radii are different from the distances between the equivalent ones [31–33]. In particular, the distribution function for Ni–Ni spacings in AuNi is much broader than that for Au–Ni, whereas the distribution function for Au–Au is much narrower [31]. This suggests that large Au atoms are more confined to regular fcc lattice positions, whereas smaller Cu and Ni atoms are smeared over the sites to a greater extent. Such behavior is also reflected in a positive deviation of the lattice parameter from Vegard's mixing rule. The results demonstrate that already for binary systems the approach with the use of averaged atomic sizes for estimations of elastic interactions and related strengthening can be misleading. It points out that the underlying mechanisms of these interrelationships are significantly more complex in alloys with large differences in atomic radii of constituents. Thus, Au-Cu-Ni-Pd-Pt alloys along with their four-component counterparts are very promising candidates for the microstructure–property relationship studies of the fcc HEAs and the related composition-dependent effects as well. A question of how the local atomic configurations in the compositionally complex Au-Cu-Ni-Pd-Pt alloy influence the strengthening behavior and whether a correlation between the constituent sizes and the component-dependent relaxations can be found is of great interest.

X-ray absorption spectroscopy combined with reverse Monte Carlo (RMC) simulations is a well-established approach that enables advanced and unbiased structural characterization of multi-component materials down to the atomic scale [34–37]. It provides insights into statistically-averaged arrangements of atoms and facilitates an understanding of their roles in certain macroscopic properties. Being beneficial for unravelling the similarities and differences in the local environment of individual components, this

approach can be exploited for detailed studies of alloy series that differ by one principal constituent. However, natural limitations related to electron scattering phenomena do not always enable the discussions of atomic short-range ordering in the system. Herein, we apply multi-edge EXAFS spectroscopy along with RMC-based analysis to explore peculiarities of element-specific local coordinations and component-dependent structure relaxations in the fcc single-phase equiatomic AuCuNiPdPt HEA and its four-component derivative, the AuCuNiPd medium-entropy alloy (MEA). Our study marks a step towards understanding the lattice distortions in the compositionally complex systems at the atomic scale and unravels new facts that are important for a better understanding of the underlying mechanisms of solid solution strengthening.

2 Materials and methods

2.1 Sample preparation and initial characterization

The equiatomic AuCuNiPdPt and AuCuNiPd alloys were prepared using high-purity metals: Au (4N), Pd (3N5), and Pt (4N) from Allgemeine Gold- und Silberscheideanstalt AG, Cu (5N5, VEB Spurenmetalle Freiberg/Sa.), and Ni (4N, Alfa Aesar). The initial remelting was done under argon atmosphere using an arc furnace (Arc Melter AM 200 Edmund Buehler GmbH). To ensure the homogeneity of samples, they were flipped-over and re-melted four times. Subsequently, the samples were cast into a cooled Cu-mould (6 mm in diameter and 75 mm in length), and the homogenization was done at 1100 and 1000 °C for the five-component AuCuNiPdPt and the four-component AuCuNiPd systems, respectively, for 20 h. The chosen temperatures correspond to about 90% of the solidus temperatures of these particular alloys. During the homogenization, the samples were placed in Ar-filled quartz tubes. After that, the samples were rapidly quenched in ice water to suppress decomposition. Prior studies [23, 30] have shown that samples following such a preparation route are single-phase and demonstrate a homogeneous microstructure in the nm range that was proven by XRD and atom probe tomography (APT). At the

end, samples were further cold worked by rotary swaging up to a true strain of $\varepsilon = 0.71$ (in three steps of $\Delta\varepsilon \approx 0.24$), and finally, recrystallization was done at homogenization temperature mentioned above for each particular alloy for 1 h followed by fast quenching in ice water. The temperatures for recrystallisation had to be that high in order to prevent decomposition which is likely to occur at lower temperatures commonly utilised for recrystallisation heat treatments. To eliminate the top deformation layer the samples were subjected to mechanical grinding with SiC paper from P400 to P2500 grit, and then polished with diamond suspension with a grit size of 3, 1, and 0.25 μm as the final step. In this way, the possible short-range order could be expected to be non-disturbed even at the surface of the sample.

The composition of the samples was verified with the use of inductively coupled plasma optical emission spectrometry after dissolving them in aqua regia: For the AuCuNiPdPt and AuCuNiPd alloys the composition was determined as $Au_{20.2}Cu_{20.1}Ni_{19.9}Pd_{20.0}Pt_{19.7}$ (at.%) and $Au_{25.0}Cu_{24.8}Ni_{25.1}Pd_{25.1}$ (at.%), respectively.

Microstructural characterization done for both alloys under study with the use of backscattered electron imaging (Focused Ion Beam Helios 600i) revealed the grain sizes in the order of 100 μm, as was observed for these alloys before. The XRD characterization of both alloys was done at the P07 beamline [38] of the large-scale synchrotron radiation facility PETRA III (Deutsches Elektronen-Synchrotron, Hamburg) with a linearly polarized X-ray photons with energy of 102.69 keV. X-ray diffraction patterns (Fig. 1) were acquired using a two-dimensional (2D) detector (XRD 1622, PerkinElmer), a beam size of 1 mm × 1 mm, and a sample-to-detector distance of approx. 1365 mm at room temperature (RT). LaB_6 powder samples were used as a calibration reference. The unit cell parameters were determined using the Rietveld method implemented in MAUD diffraction software [39, 40]; the structural model was described by the fcc cell belonging to the space group $Fm\bar{3}m$. The experimental lattice parameters were found to be 3.8250 Å for AuCuNiPdPt HEA and 3.8025 Å for AuCuNiPd MEA, respectively, and were further used for the initial supercell construction necessary in the RMC-based analysis.
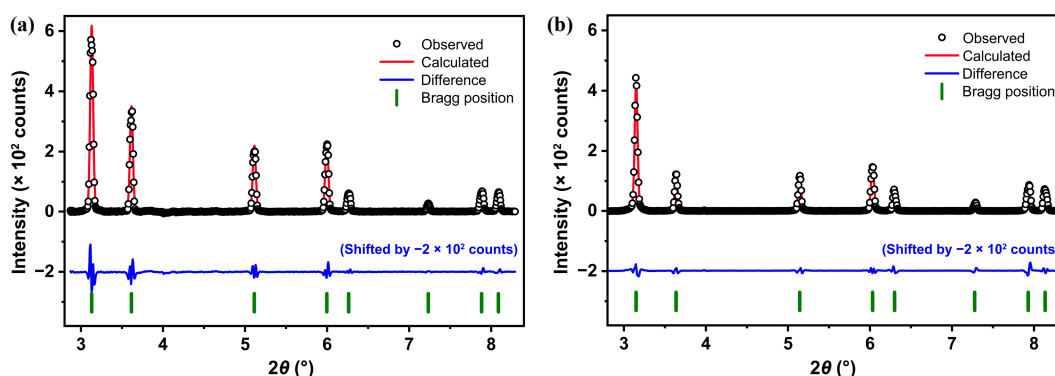

Figure 1 Rietveld refinement (solid red line) of the X-ray diffraction patterns (open circles) for (a) AuCuNiPdPt HEA and (b) AuCuNiPd MEA. The vertical green bars indicate the positions of the Bragg reflections for the fcc lattice. Solid blue line shows the difference between the measured and calculated XRD patterns.

2.2 Multi-edge X-ray absorption spectroscopy

X-ray absorption spectra from AuCuNiPdPt and AuCuNiPd alloys (Fig. 2) were recorded at the K-absorption edges of Ni (8.3 keV), Cu (8.9 keV), and Pd (24.35 keV), as well as at the L_3-absorption edges of Pt (11.56 keV) and Au (11.92 keV) at the P65 mini-

undulator (11 periods) beamline at DESY PETRA III synchrotron radiation facility [41]. The fluorescent yield (FY) was collected using the 4-elements silicon drift diode (SDD) fluorescence detector (Hitachi ME4) after the initial excitation with horizontally polarized X-ray photons. The samples in the form of ~ 4.5 mm discs were
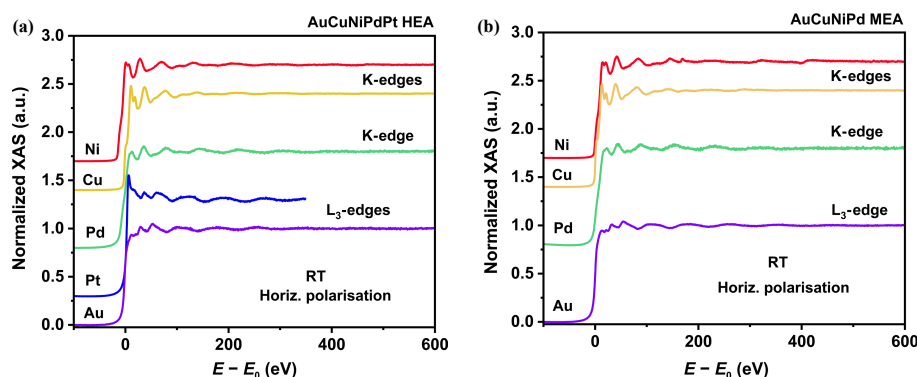
Figure 2 The normalized X-ray absorption spectra collected at the K-absorption edges of Ni (8.3 keV), Cu (8.9 keV), and Pd (24.35 keV), as well as at the L_3-absorption edges of Pt (11.56 keV) and Au (11.92 keV) at RT using fluorescence yield and 45° incidence geometry for AuCuNiPdPt high-entropy (a) and AuCuNiPd medium-entropy (b) alloys. E_0 was determined as the energy corresponding to the first maximum of the first derivative of each spectrum. Spectra are normalized to unity and shifted vertically for clarity. For the Pt L_3-absorption edge, only a limited EXAFS region is assessable due to the closeness of the Au L_3-edge.

fixed in the primary X-ray beam (1 mm (horiz.) × 0.5 mm (vert.)) with the use of Kapton foil in the 45° incident geometry; the X-ray flux on the sample was in the range of 10^{10} photons·s^{-1}. All measurements were performed at RT.

The intensity of the incoming X-ray photons was monitored using the first ionization chamber filled in with N_2 and Ar in proportion 70:30 (to get approx. 10% of absorption) for energies below 20 keV (K-edges of Ni and Cu, and L_3-edges of Pt and Au), and with N_2 and Kr in proportion 80:20 for energies above 20 keV (Pd K-edge), respectively. Two water-cooled double crystal monochromators with Si(111) crystals (along with a Si mirror for energies below 20 keV) or Si(311) crystals (along with a Pt-coated Si mirror for the Pd K-edge) were employed.

As references, X-ray absorption spectra of pure Au, Cu, Ni, Pd, and Pt foils were recorded at room temperature in transmission. The second ionization chamber was filled in with N_2 and Ar in proportion 40:60 (to get approx. 50% of absorption) and with N_2 and Kr in proportion 65:35 for energies below and above 20 keV, respectively.

The raw data were pre-processed (in terms of necessary normalization, corrections, and integration) and averaged over the individual channels of the corresponding fluorescence detector. The EXAFS spectra $\chi(k)k^2$ needed for the RMC analysis were then extracted from the averaged raw data using a conventional procedure [42] implemented in the X-ray absorption and emission spectroscopy analytics (XAESA) code [43]. The EXAFS spectra recorded at the K-absorption edges of Ni, Cu, and Pd, and L_3-absorption edges of Pt and Au were used in the RMC simulations. The self-absorption effects were found to be negligible in the energy range chosen for the fitting procedure.

2.3 RMC simulations

The possibility to unbiasedly fit one and the same structural model simultaneously to several EXAFS spectra collected at the X-ray absorption edges of principal components in a multi-component system is one of the main advantages of RMC-based data analysis. In our work, the RMC approach implemented in the EvAX code was employed [44, 45]. The comparison between the experimental and calculated EXAFS spectra was done simultaneously in k and R spaces [46] with the help of the wavelet transforms (WTs) for better accounting of the existing differences in electron scattering amplitudes for all types of backscatters. The evolutionary algorithm (EA) was applied for the acceleration of the optimization procedure [44]. It includes three operations: selection, crossover, and mutation, which were applied to sets of atomic configurations at

each step of RMC simulation, significantly accelerating the convergence of the structural model. The details of the method are provided in Ref. [44].

To start the RMC-based analysis, the simulation box was built as a $4a \times 4a \times 4a$ supercell employing the periodic boundary conditions (PBC) with the experimental value of the fcc lattice parameter $a = 3.8250$ Å for AuCuNiPdPt HEA (or $a = 3.8025$ Å for AuCuNiPd MEA) determined by XRD. The Au, Cu, Ni, and Pd (and Pt) atoms (256 in total) were randomly distributed in a proper concentration (20 at.% for each element in AuCuNiPdPt or 25 at.% for each element in AuCuNiPd) at the Wyckoff positions of the fcc lattice. The size of the simulation box was kept constant during the simulations. The number of atomic configurations simultaneously considered in the EA algorithm was 32 [44]. In this study, we followed the same procedure as described previously in Refs. [34–36], where more details about the general benefits of the RMC method as compared to conventional multi-shell EXAFS analysis, the detailed requirements for the construction of the initial simulation box, the simulations, and the main procedure at each iteration step can be additionally found. Due to rather large grain sizes for both alloys, the simulations were performed without taking into account a possible influence of the grain boundaries, which were assumed to be negligible.

At each RMC iteration, the configuration-averaged EXAFS (CA-EXAFS) spectra $\chi(k)k^2$ were calculated over all Au, Cu, Ni, and Pd (and Pt) atoms in the constructed simulation box using *ab initio* real-space multiple-scattering FEFF8.50L code [47, 48] including the multiple scattering (MS) effects up to the fourth order, and their Morlet WTs were compared with those of the experimental EXAFS spectra. The best agreement between the WTs of the experimental and calculated CA-EXAFS spectra was used as a criterion for the model structure optimization. The total number of RMC iterations was 5000 to guarantee the convergence of the structural model.

The WTs calculations were performed in the k-space and R-space ranges for AuCuNiPdPt and AuCuNiPd alloys, as presented in Table 1. As a result of each RMC simulation, a set of final atomic coordinates was obtained, which was further used to calculate the pair distribution functions (PDFs) $g(r)$. The statistically-averaged mean interatomic distances $<R>$ and the mean square relative displacements (MSRDs) for each pair of atoms were evaluated, respectively, as the first and second moments of the PDFs $g(r)$, while the mean square displacements (MSDs) for atoms of each type were determined from the coordinates of atoms (Tables 3–6). Note that the MSRD provides information on the correlated

motion of atoms, while the MSD includes only uncorrelated effects as in the case of diffraction techniques [49]. Moreover, both MSD and MSRD include also contributions from structural (static) distortions due to atom relaxations. To improve statistics, 20 sets of

different (independent) starting structural models were considered for the final averaged PDFs. For both alloys, the Warren–Cowley short-range order parameter is zero in each structural model due to the random distribution of atoms throughout the simulation box.

Table 1 The k- and R-space ranges used in the RMC-based analysis to simultaneously fit the K-edge (Cu, Ni, and Pd) and L_3-edges (Pt and Au) EXAFS spectra of AuCuNiPdPt and AuCuNiPt alloys

		Au	Cu	Ni	Pd	Pt
AuCuNiPdPt (fluorescence yield)	k-space	3–11 Å⁻¹	3–12 Å⁻¹	3–12 Å⁻¹	3–11 Å⁻¹	3–9.5 Å⁻¹
	R-space			1–6 Å		
AuCuNiPd (fluorescence yield)	k-space	3–11 Å⁻¹	3–12 Å⁻¹	3–8.5 Å⁻¹ᵃ	3–11 Å⁻¹	—
	R-space			1–6 Å		

[a] A shorter fitting range for Ni in AuCuNiPd MEA as compared to AuCuNiPdPt HEA is related to the presence of two glitches at $k = 6.5$ Å⁻¹ and $k = 10$ Å⁻¹.

Table 2 Lattice parameters (a), calculated radii ($r = \frac{\sqrt{2}}{4} \cdot a$), shear ($G$), and Young's ($E$) modulus of the pure elements, taken from Ref. [50]

	a (Å)	r (Å)	G (GPa)	E (GPa)
Au	4.0782	1.4419	27	78
Pt	3.9242	1.3874	61	168
Pd	3.8907	1.3756	44	121
Cu	3.6149	1.2781	48	130
Ni	3.5241	1.2459	76	200

Table 3 Component-dependent structural parameters ($<R>$, MSD, and MSRD) for AuCuNiPdPt HEA at 300 K. The MSD values were calculated from the coordinates of atoms, while the MSRD values were extracted from the total PDFs. The error bars for the $<R>$ values are ±0.02 Å in all cases

	Average distances $<R>$ for the first/second coordination shells (Å)	MSD (Å²) (from coordinates)	MSRD (Å²) (from total PDFs)
Au	2.72/3.83	0.025 ± 0.002	0.017 ± 0.002
Pt	2.71/3.83	0.023 ± 0.002	0.017 ± 0.002
Pd	2.72/3.83	0.027 ± 0.002	0.020 ± 0.002
Cu	2.71/3.83	0.034 ± 0.003	0.024 ± 0.002
Ni	2.71/3.83	0.035 ± 0.003	0.025 ± 0.002

$\Delta R_1 = 2.3$–3.2 Å and $\Delta R_2 = 3.4$–4.2 Å. Distances from XRD: 2.705 Å (1st shell) and 3.825 Å (2nd shell).

Table 4 Component-dependent structural parameters ($<R>$, MSD, and MSRD) for AuCuNiPd MEA at 300 K. The MSD values were calculated from the coordinates of atoms, while the MSRD values were extracted from the total PDFs. The error bars for the $<R>$ values are ±0.02 Å in all cases

	Average distances $<R>$ for the first/second coordination shells (Å)	MSD (Å²) (from coordinates)	MSRD (Å²) (from total PDFs)
Au	2.70/3.83	0.023 ± 0.002	0.018 ± 0.002
Pd	2.71/3.81	0.030 ± 0.002	0.023 ± 0.002
Cu	2.70/3.81	0.032 ± 0.003	0.025 ± 0.002
Ni	2.70/3.81	0.033 ± 0.003	0.025 ± 0.002

$\Delta R_1 = 2.3$–3.2 Å and $\Delta R_2 = 3.4$–4.2 Å. Distances from XRD: 2.6888 Å (1st shell) and 3.8025 Å (2nd shell).

Table 5 Component-dependent structural parameters (MSRD and MSD for the first coordination shell) for AuCuNiPdPt HEA at 300 K. The MSD values were calculated from the coordinates of atoms, while the MSRD values were extracted from the partial PDFs. The error bars for the MSD and MSRD values are ±0.003 Å² in all cases

MSRD (Å²) (from partial PDFs)	Au	Pt	Pd	Cu	Ni	MSD (Å²) (from coordinates)
Au	0.016	0.013	0.017	0.020	0.019	0.025
Pt		0.013	0.018	0.020	0.021	0.023
Pd			0.022	0.020	0.022	0.027
Cu				0.027	0.031	0.034
Ni					0.031	0.035

Table 6 Component-dependent structural parameters (MSRD and MSD for the first coordination shell) for AuCuNiPd MEA at 300 K. The MSD values were calculated from the coordinates of atoms, while the MSRD values were extracted from the partial PDFs. The error bars for the MSD and MSRD values are ±0.003 Å² in all cases

MSRD (Å²) (from partial PDFs)	Au	Pd	Cu	Ni	MSD (Å²) (from coordinates)
Au	0.014	0.018	0.020	0.018	0.023
Pd		0.029	0.022	0.021	0.030
Cu			0.027	0.031	0.032
Ni				0.030	0.033

3 Results

The averaged local environment of each principal component was probed by element-specific X-ray absorption spectroscopy at the K- or L_3-absorption edges of constituents. The shape, positions, and amplitudes of EXAFS oscillations found above each absorption edge reflect the local coordination of each type of atom in the crystallographic lattice. The normalized X-ray absorption spectra recorded at RT for the AuCuNiPdPt and AuCuNiPt alloys are shown in Fig. 2 and demonstrate very similar EXAFS oscillations for the same principal components in both systems. Nevertheless, the shape of oscillations found above Ni, Cu, and Pd K-edges looks to be different from those found above Pt and Au L_3-edges, indicating the difference in the local (short-range) environment of these groups of atoms. The possible contributions from the sub-surface oxide layer to the collected X-ray absorption spectra can be neglected due to the relatively large probing depth of FY detection mode in the considered energy ranges (approx. 8–40 μm).

A reliable three-dimensional (3D) structural model of the material can be extracted from the collected experimental EXAFS data with the use of the RMC-based fitting procedure accounting for static and dynamic lattice relaxations. In general, despite only a limited number of initial configurations that can be considered during the RMC simulations, the RMC-based analysis affords a set of pair distribution functions $g(r)$ that describe the most significant statistically-averaged peculiarities of atom distributions within the several first coordination shells of absorbers of each type [34–36].

An example of the initial (starting) and final (relaxed) configurations of atoms used in the simulation boxes for the AuCuNiPdPt and AuCuNiPt alloys during the RMC-based analysis are shown in Figs. 3 and 4, respectively. The particular structural models were simultaneously fitted to available EXAFS spectra independently collected at the K- and L_3-absorption edges for each alloy. The atomic coordinates obtained for all relaxed atoms in the constructed supercells were further used to calculate the total and partial component-specific PDFs.

The experimental and RMC-fitted EXAFS spectra for both systems are shown in Figs. 5 and 6, correspondingly, together with their Fourier transforms (FTs) and WTs. The RMC-fitted data reproduce well the experimental data in both k and R spaces at all considered absorption edges and demonstrate visible dissimilarities in FTs related to Ni/Cu and Pt/Au groups of atoms; FTs for Pd demonstrate an intermediate situation. Such a reproducibility of the experimental data by the fitted ones suggests that the final structural model based on atoms randomly distributed over the supercell is self-consistent.

As discussed earlier [35, 37], in the special case of the fcc structure, where the first peak in the FTs of the experimental EXAFS data is well isolated and located between 1.0 and 3.5 Å (Figs. 5 and 6), any further quantitative estimations related to the
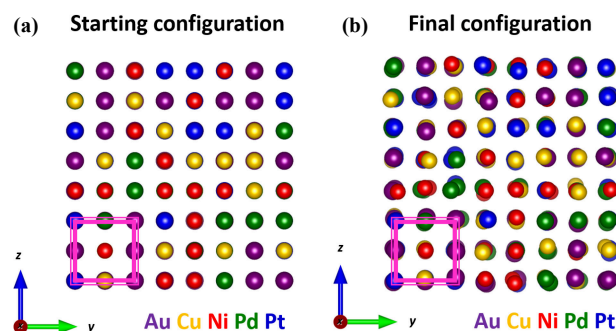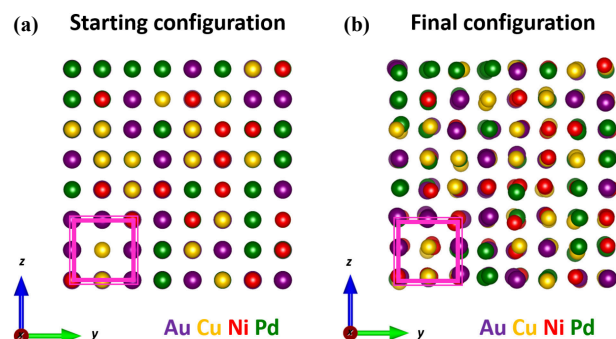

Figure 3 Examples of (a) starting (initial) and (b) final atom configurations (simulation boxes) used in the RMC simulations for simultaneous fit to the EXAFS spectra of the AuCuNiPdPt high-entropy alloy at five absorption edges (Au, Cu, Ni, Pd, and Pt) at 300 K. The initial simulation box (a) was randomly filled with atoms according to the alloy composition; periodic boundary conditions were applied to minimize the influence of surface effects. Colour scheme: Au (purple), Cu (gold), Ni (red), Pd (green), and Pt (blue). The top views of the simulation boxes are shown along the z-direction in chosen xyz coordinates as depicted. The schematic border of the fcc unit cell is displayed for both configurations.

Figure 4 Examples of (a) starting (initial) and (b) final atom configurations (simulation boxes) used in the RMC simulations for simultaneous fit to the EXAFS spectra of the AuCuNiPd medium-entropy alloy at four absorption edges (Au, Cu, Ni, and Pd) at 300 K. The initial simulation box (a) was randomly filled with atoms according to the alloy composition; periodic boundary conditions were applied to minimize the influence of surface effects. Colour scheme: Au (purple), Cu (gold), Ni (red), and Pd (green). The top views of the simulation boxes are shown along the z-direction in chosen xyz coordinates as depicted. The schematic border of the fcc unit cell is displayed for both configurations.

nearest-neighbors around absorbers of each type have eligible accuracy and thus assured. So, the extracted *total* PDFs represent the most essential details of the nearest-neighbour arrangements in the first coordination shell of the corresponding absorbers.

For compositionally complex systems, the RMC-based approach allows for performing a reliable analysis of the available experimental EXAFS spectra in the most unbiased manner without
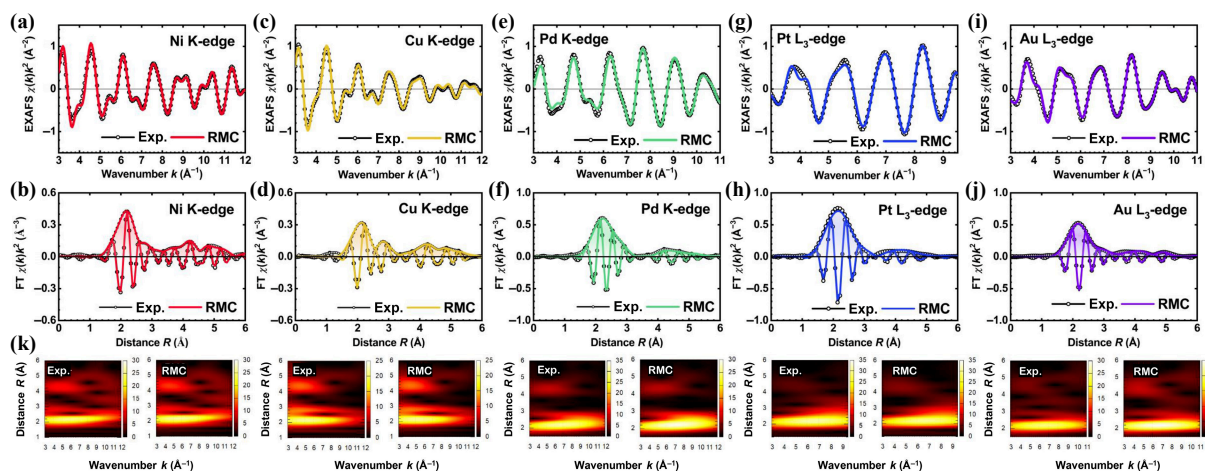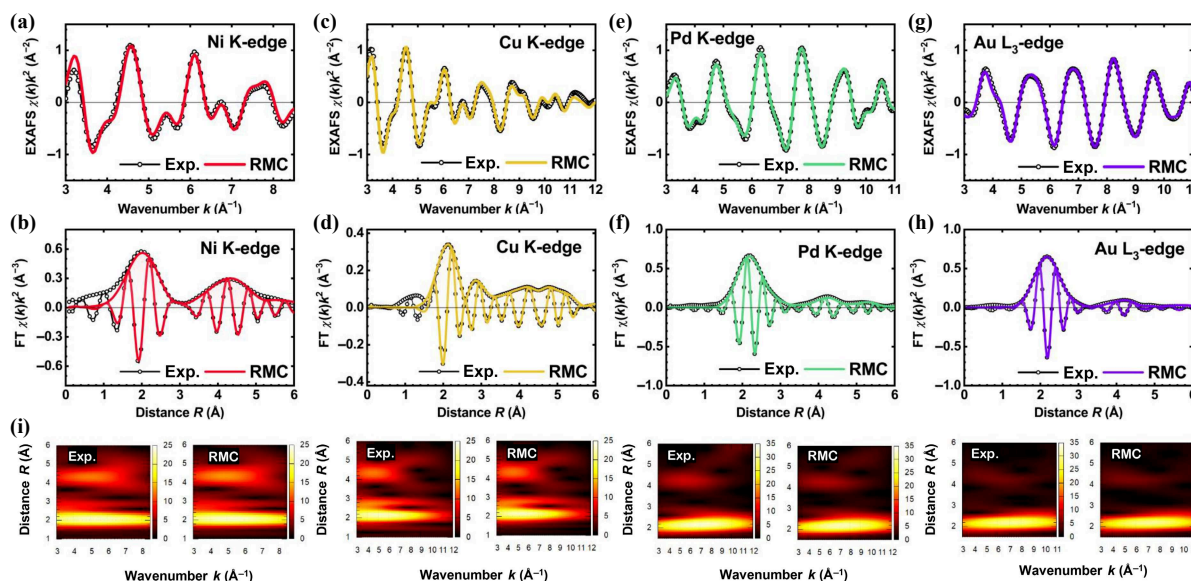
Figure 5 Experimental (black dots and lines) and RMC-calculated (coloured lines) EXAFS spectra $\chi(k)k^2$ of (a) Ni (K-edge), (c) Cu (K-edge), (e) Pd (K-edge), (g) Pt (L$_3$-edge), and (i) Au (L$_3$-edge), as well as their (b), (d), (f), (h), (j) FTs and (k) WTs for the AuCuNiPdPt high-entropy alloy at 300 K.

Figure 6 Experimental (black dots and lines) and RMC-calculated (coloured lines) EXAFS spectra $\chi(k)k^2$ of (a) Ni (K-edge), (c) Cu (K-edge), (e) Pd (K-edge), and (g) Au (L$_3$-edge), as well as their (b), (d), (f), (h) FTs and (i) WTs for the AuCuNiPd medium-entropy alloy at 300 K.

any additional assumptions about probable interrelations between fitted parameters. Reconstruction of the local environment is possible at least in the first five coordination shells around each type of absorber (distances up to 6.0 Å). The displacements of atoms present in the final configurations account for both thermal (dynamic) and structural (radial and angular) disorders.

The sensitivity of EXAFS oscillations as well as the reconstructed structural models to the local environment around absorbers in the compositionally complex systems depends, in particular, on the differences in the scattering amplitudes $F(k)$ of neighbouring atoms acting as backscatters. Due to a difference between scattering amplitudes of Ni/Cu, Pd, and Pt/Au (see Fig. 7), these three groups of significantly distinct atoms can be identified and distinguished in AuCuNiPdPt and AuCuNiPd alloys according to their contributions to the EXAFS spectra more precisely than in the case of the Cantor alloy where all 3d principal components behave as backscatters in a very similar way.

A set of total PDFs calculated from the atomic coordinates of the final structural models for the AuCuNiPdPt and AuCuNiPt alloys is shown in Fig. 8. Each of these PDFs is a component-specific
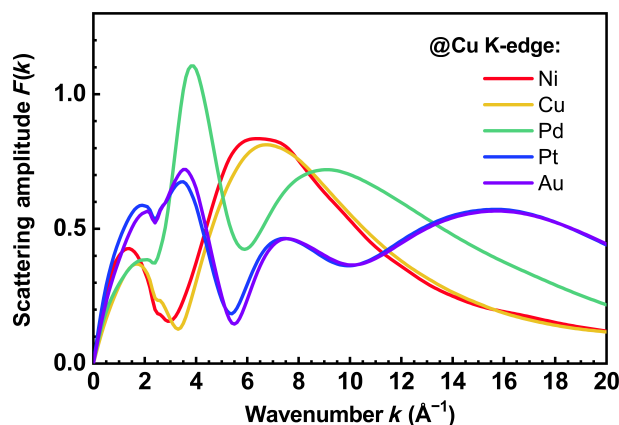

Figure 7 Illustration of the scattering amplitudes $F(k)$ employed in the RMC calculations that are associated with elements acting as backscatters around Cu absorbers in the considered AuCuNiPdPt HEA. Three different groups of curves—Ni/Cu, Pd, and Pt/Au—are clearly notable. Nevertheless, within each particular group further distinguishing is hardly possible.

projection of the three-dimensional structure of the studied fcc alloy over a radial distance relative to the corresponding absorbing atom and describes the configuration-averaged local environment around a particular absorber. For both alloys, the principal components demonstrate total PDFs with the same number and positions of peaks within the first five coordination shells, corresponding to a distribution of all types of atoms over the equilibrium fcc lattice positions.

At the same time, a clear shift towards shorter distances and pronounced asymmetry of the first peaks in total PDFs of Ni and Cu for both alloys are visible, while the first peaks of Pt and Au PDFs are much more symmetric and do not demonstrate such a shift. The Pd PDFs demonstrate an intermediate situation. The asymmetry of the PDFs maxima for Ni and Cu atoms is also visible for their second coordination shells in both alloys, but it vanishes for more distant shells pointing out the importance of short-range variations of the local atom arrangements in the considered systems.

For the AuCuNiPdPt HEA total PDFs maxima related to the first coordination shell around Ni and Cu absorbers are visibly asymmetric and are shifted to shorter distances (2.64 and 2.66 Å, correspondingly) as compared to the average distance $<R>$ (2.71 Å). The same maximum for Pd is less asymmetric, and those for Pt and Au are almost symmetric. The positions of PDFs maxima for Pd and Pt coincide with the average distance (2.70 Å), whereas the maximum of Au PDF is slightly shifted to a longer distance (2.73 Å). For the AuCuNiPd MEA total PDFs maxima related to the first coordination shell around Ni, Cu, and Pd are asymmetric with a clear shift to shorter distances (2.63, 2.64, and 2.65 Å, correspondingly) as compared to the average distance (2.70 Å), whereas the same maximum of the total PDF for Au is more symmetric. The position of Au PDF maximum coincides with the average distance (2.70 Å). The obtained differences in shifts and asymmetries correlate well with the increased radii of metal atoms in the fcc structure: r(Ni) = 1.24 Å, r(Cu) = 1.28 Å, r(Pd) = 1.37 Å, r(Pt) = 1.39 Å, and r(Au) = 1.44 Å (see Table 2).

The component-dependent MSD values were calculated directly from the coordinates of atoms according to the final (relaxed) configurations of the AuCuNiPdPt and AuCuNiPd alloys, whereas the mean interatomic distances $<R>$ and MSRD values were calculated as the first and second moments of the total PDFs for atoms of each type (Tables 3 and 4). For both alloys, the average distances in the first and second coordination shells of all principal components are almost the same and agree with the values

extracted from XRD: 2.71–2.72 Å/3.83 Å for the AuCuNiPdPt HEA, and 2.70–2.71 Å/3.81–3.83 Å for the AuCuNiPd MEA, correspondingly.

For the AuCuNiPdPt HEA, the MSD values calculated from coordinates of atoms with larger radii such as Au, Pt, and Pd are in the range of 0.023–0.027 Å^2 and are significantly smaller than those for smaller atoms such as Cu and Ni (0.034–0.035 Å^2). The MSRD values related to the first coordination shell and calculated as second moments from the total PDFs are also the smallest for Au and Pt atoms (0.017 Å^2), exhibit an intermediate value for Pd (0.020 Å^2), and are the largest for Cu and Ni atoms (0.024–0.025 Å^2). This tendency remains also in the second coordination shell but is less pronounced: 0.021 Å^2 for Au/Pt and 0.024 Å^2 for Pd/Cu/Ni. For the AuCuNiPd MEA, the MSD value calculated from coordinates of Au atoms with a larger radius is equal to 0.023 Å^2 and is significantly smaller than the MSD values for smaller atoms such as Pd, Cu, and Ni (0.030–0.033 Å^2). The MSRD values related to the first coordination shell and calculated as second moments of the total PDFs are the smallest for Au (0.018 Å^2), have an intermediate value for Pd (0.023 Å^2), and are the largest for Cu and Ni (0.025 Å^2). In the second coordination shell, this tendency remains but is less pronounced: 0.022 Å^2 for Au, and 0.025–0.027 Å^2 for Pd/Cu/Ni. So, the MSD and MSRD values calculated from total PDFs for all components in both alloys demonstrate a strong correlation with the radii of metal atoms in the fcc structure, directly highlighting a significant and dominant effect of the metal atoms radii on the local structure relaxations.

The availability of atomic coordinates in the final configurations allows one to calculate also *partial* PDFs (Figs. 9 and 10). The MSRDs for each pair of atoms were also calculated as the second moments of the partial PDFs (see Tables 5 and 6). The smallest MSRDs found for the AuCuNiPdPt HEA from partial PDFs are in the range of 0.013–0.016 Å^2 for the Au–Au, Au–Pt, and Pt–Pt pairs (the pairs of the largest atoms), while the significantly larger MSRDs (0.027–0.031 Å^2) were found for Cu–Cu, Cu–Ni, and Ni–Ni pairs of the smaller atoms. Pd–Pd pairs demonstrate an intermediate MSRD value (0.022 Å^2). For AuCuNiPd MEA the MSRD value found for Au-Au pairs is the smallest one (0.014 Å^2), while the MSRDs for all other pairs of smaller atoms (Cu–Cu, Cu–Ni, Ni–Ni, and Pd–Pd) are larger (0.027–0.031 Å^2). Interestingly, in the case of AuCuNiPd MEA (a four-component alloy in the absence of Pt), the Pd–Pd PDF is the most affected, and the Pd–Pd pairs exhibit a very large MSRD value and do not demonstrate an intermediate situation as in the case of five-component AuCuNiPdPt HEA alloy.
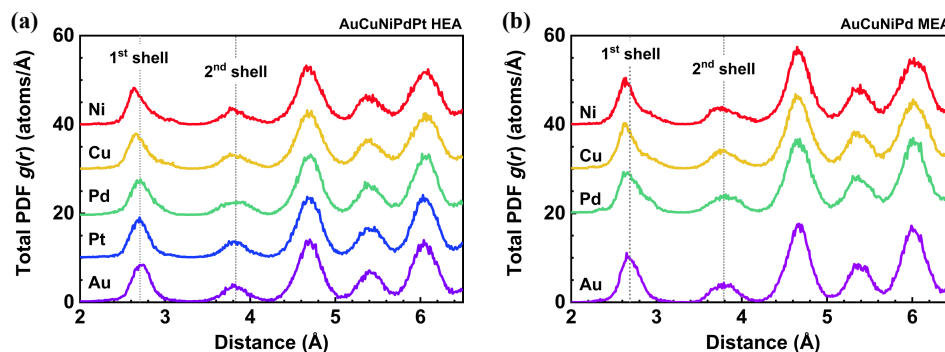

Figure 8 Total pair distribution functions $g(r)$ for the AuCuNiPdPt high-entropy (a) and AuCuNiPd medium-entropy (b) alloys at 300 K extracted from the RT EXAFS spectra $\chi(k)k^2$ of Ni (K-edge), Cu (K-edge), Pd (K-edge), Pt (L$_3$-edge), and Au (L$_3$-edge), respectively, using the RMC method. Curves are shifted vertically for clarity. The strong asymmetry of the peaks related to the first coordination shell is visible only for Ni and Cu whereas those peaks for Au and Pt are much more symmetric. The same peak for Pd demonstrates an intermediate case with only a small asymmetry.
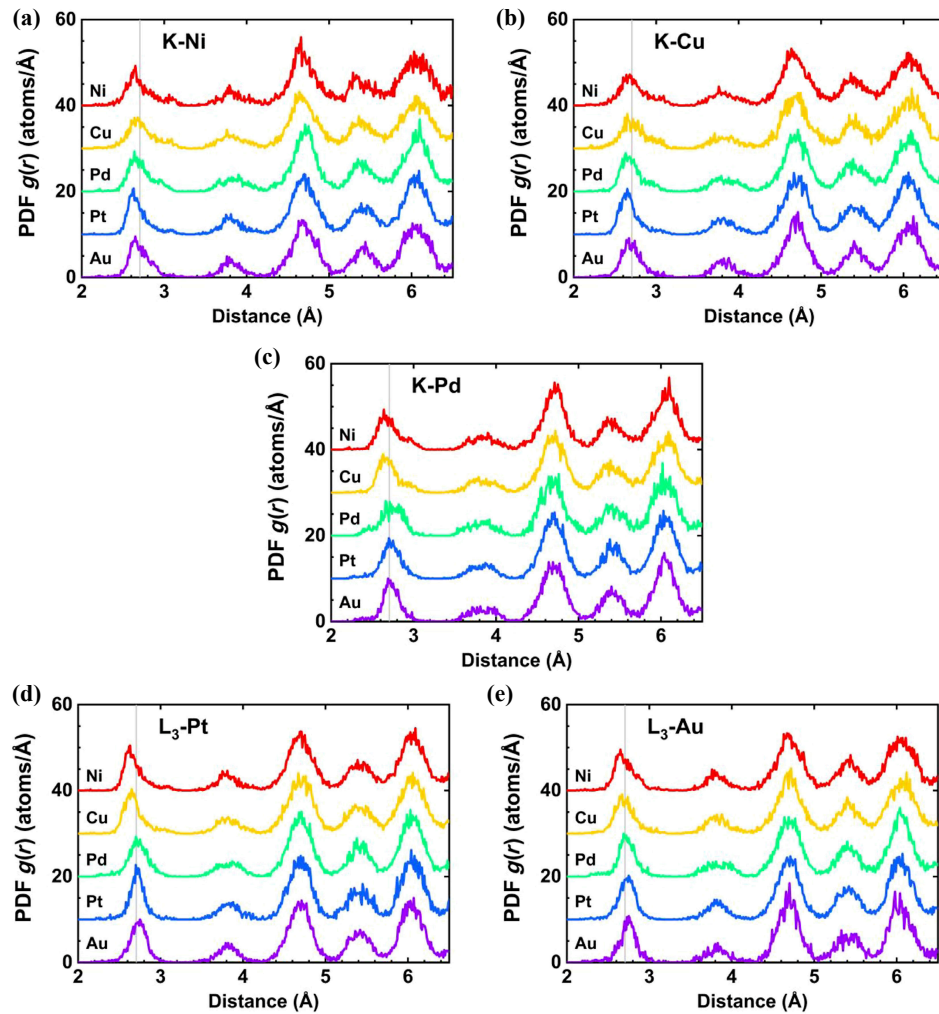
Figure 9 Partial pair distribution functions $g(r)$ for the AuCuNiPdPt high-entropy alloy at 300 K extracted from the RT EXAFS spectra $\chi(k)k^2$ of (a) Ni (K-edge), (b) Cu (K-edge), (c) Pd (K-edge), (d) Pt (L_3-edge), and (e) Au (L_3-edge) using the RMC method. Curves are shifted vertically for clarity.
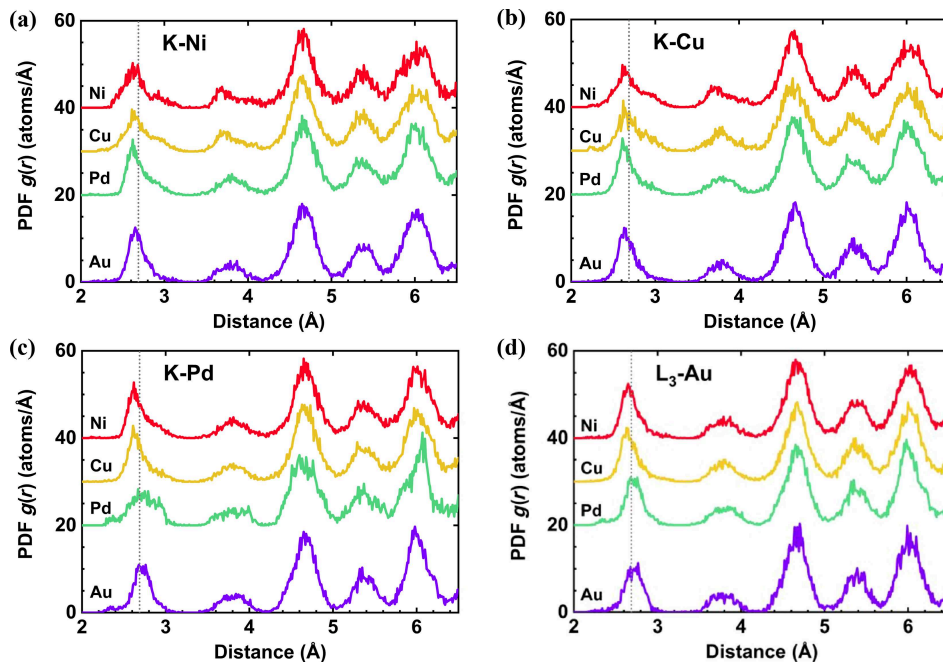

Figure 10 Partial pair distribution functions $g(r)$ for the AuCuNiPd medium-entropy alloy at 300 K extracted from the RT EXAFS spectra $\chi(k)k^2$ of (a) Ni (K-edge), (b) Cu (K-edge), (c) Pd (K-edge), and (d) Au (L_3-edge) using the RMC method. Curves are shifted vertically for clarity.

Thus, according to the results of the RMC-based analysis, a clear difference in the first coordination shell between three groups of atoms—Ni/Cu, Pd, and Pt/Au—is visible both in partial and total PDFs for the AuCuNiPdPt HEA whereas AuCuNiPd MEA demonstrates some variations from this tendency.

The results obtained from the experimental EXAFS data using the RMC-based analysis can be further compared with those from molecular dynamic (MD) simulations reported by Takeuchi et al. [51]. The simulations were conducted for both fcc AuCuNiPdPt HEA and AuCuNiPt MEA at T = 1000 K, revealing larger MSDs for all atoms in the alloys: In the AuCuNiPdPt HEA MSDs were ~ 0.4 Å² for Cu/Ni, ~ 0.3 Å² for Pd, and ~ 0.2 Å² for Au/Pt [51]. These values are about ten times larger than those found in our work, which can be attributed to the significantly higher temperature used for the MD simulations compared to the RT EXAFS experiment. However, the relative order of the MSD values is similar to our results (shown in Table 3), suggesting that the smallest atoms exhibit the largest MSDs.

4 Discussion

The local lattice distortions experimentally explored in the chemically complex AuCuNiPdPt HEA and AuCuNiPd MEA with the use of EXAFS spectroscopy in combination with RMC-based analysis have demonstrated a number of peculiarities that can be further used to refine common approaches in the description of multi-principal-component system properties. The alloys under investigation were revealed to be single-phase at the atomic scale, confirming earlier observations that the applied processing route leads to a homogenous distribution of the constituents at the nm scale as it was evaluated by atom probe tomography measurements [23, 30]. Thus, these alloys can be recognised as suitable model systems for studying different interrelationships between local atomic displacements and macroscopic properties.

The most foreseen outcome of our work is that atomic displacements, MSDs, of small atoms (Cu/Ni) in the fcc lattice are pronouncedly larger than those of larger atoms (Au/Pt). At the same time, the MSD value of Pd is close to those of Cu/Ni in MEA but is closer to the MSD values of Au/Pt in HEA. Also, the MSRD values for Ni–Ni, Ni–Cu, and Cu–Cu small atom pairs are visibly larger as compared to those for Au–Au, Au–Pt, and Pt–Pt large atom pairs, implying that large atoms (Au/Pt) are more confined on the regular lattice positions whereas the small atoms (Cu/Ni) are more displaced. These results indicate that the average matrix model based on the concentration-weighted parameters of all components is not fully applicable to alloys with large differences in sizes of the elements, and can be used only to a certain extent since atoms of each type occupy the equilibrium lattice positions not in the same manner.

Macroscopically, this situation is reflected in a slightly positive deviation of the experimentally found lattice parameters from the theoretically estimated ones: According to Vegard's law and considering the size of the fcc unit cell for pure elements (see Table 2), the theoretical lattice parameters expected for AuCuNiPdPt HEA and AuCuNiPd MEA are 3.8065 and 3.7770 Å, correspondingly. Meanwhile, the experimentally found values from XRD are 3.8250 (for HEA) and 3.8025 Å (for MEA), yielding positive deviations of +0.019 and +0.026 Å for both alloys, respectively. It demonstrates that Vegard's law is not strictly valid in predicting the lattice parameters for alloys with high differences in

atomic sizes. This behavior is already known for binary alloys such as AuCu, AuNi, and CuPt [52]. Considered as a function of the composition, this deviation is the largest for the equimolar AuNi and CuPt alloys and decreases on both sides of the binary phase diagrams towards the pure elements. EXAFS studies performed by Renauld et al. [31] and Lu et al. [33] have stated that in these binary systems, large Au atoms are more rigid on the nodes of the regular lattice positions whereas small Ni/Cu atoms can move further away from the ideal positions in the same fcc lattice. Now we have demonstrated that this effect is also present in the much more chemically complex AuCuNiPdPt alloy as well as in its quaternary AuCuNiPd derivative.

Furthermore, in Fig. 11, the experimentally found MSDs of the principal components are plotted vs. the atomic radii r estimated from the lattice parameters of pure elements (Table 2). It turns out that the atomic displacements are systematically influenced by the size of the elements. The observed peculiarity for Pt atoms which demonstrate smaller displacements than the larger Au atoms could be due to the comparatively lower Young's and shear modulus of Au as compared to other components. This relationship is supported by Ye et al. [2], who suggested that elastic modulus misfit generally results in lattice distortions. This complies with the traditional approach to SSS, where both parelastic and dielastic interactions are considered. These displacements were also discussed in terms of local charge transfer between different elements and different orbitals of the same atom (see, e.g., Ref. [53]). This may cause a stronger deflection of Au atoms from their ideal lattice positions, despite their larger radius.
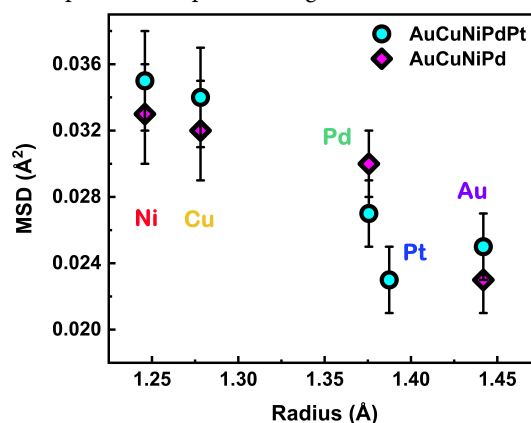

Figure 11 MSDs of principal components in AuCuNiPdPt and AuCuNiPd alloys depending on the atomic radius estimated for pure elements.

The most intriguing finding of our work is a visible shift of the first PDF maxima and a pronounced asymmetry of PDFs for particular principal components in the alloys studied. These quantities were not seen previously in different forms of Cantor alloy [34–37].

The experimental mean interatomic distance $\langle R \rangle$, calculated as the first moment of the total PDF peak related to the first coordination shell, usually coincides with the position of the first total PDF peak maximum (R_{PDFmax}). However, in the case of strong lattice distortions these two quantities seem to vary: Despite $\langle R \rangle$ value should stay constant due to the defined unit cell size over the material, the preferential statistically-averaged positions of particular atoms within the unit cell can still be shifted. Intuitively, it is clear that if atoms of pronouncedly different sizes belong to the same unit cell, the preferential shifts of the total PDF maxima are

expected to maintain the density of lattice packing. Meanwhile, the theoretically estimated interatomic distances can be calculated pairwise by applying the hard-sphere model with the use of atomic radii of the corresponding elements (see Table 2). In the case of a random element distribution (as currently assumed for the considered HEA and MEA), the theoretical mean interatomic distance (d_{Vegard}) is supposed to be an average over distances of all individual pairs. This value, further compared with the observed position of the first total PDF maxima, will demonstrate whether notable differences between theoretical estimations and experiment are present.

The anticipated change of the Goldschmidt radii of constituents due to different atomic surroundings is assumed to be 0.03 Å at most. However, as it can be seen from Table 7 for AuCuNiPdPt HEA, the d_{Vegard} values of Au, Cu, and Ni demonstrate stronger deviations ($\Delta = d_{Vegard} - R_{PDFmax}$). The observed R_{PDFmax} of Au is lower (2.73 Å) than the expected d_{Vegard} (2.79 Å) with Δ(Au) = +0.06 Å, suggesting that Au atoms are preferentially bonded with smaller atoms. The opposite is found for Cu and Ni, which demonstrate larger R_{PDFmax} as compared to d_{Vegard}: Δ(Cu) = −0.04 Å and Δ(Ni) = −0.05 Å, suggesting that Cu and Ni are preferentially bonded with larger atoms. In the case of AuCuNiPd MEA, this effect is even more pronounced (see Table 8): Both, Au and Pd show positive deviations (Δ(Au) = +0.08 Å and Δ(Pd) = +0.06 Å), whereby Ni shows a negative deviation Δ(Ni) = −0.05 Å. Whereas Pd in AuCuNiPdPt HEA shows a good agreement between the expected average distance and the observed mean value, a visibly different situation is seen in the four-component AuCuNiPd alloy. This could be an indication that the local atomic arrangement around Pd atoms is different in AuCuNiPd MEA as compared to the five-component AuCuNiPdPt alloy. Due to the similarity of the photoelectron scattering amplitudes of Cu/Ni and Pt/Au atoms (see Fig. 7), the precise determination of atom configurations within the several first coordination shells around each type of absorber is not possible. Nevertheless, the abovementioned comparison indicates that the preferred nearest-neighbour bonding is taking place and varies depending on the alloy composition.

Table 7 Calculated interatomic distances d_{Vegard} vs. observed maximum R_{PDFmax} in the total PDFs of AuCuNiPdPt HEA together with their difference $\Delta = d_{Vegard} - R_{PDFmax}$. All values are given in Å

	Au	Pt	Pd	Cu	Ni	d_{Vegard} (calculated)	R_{PDFmax} (observed)	Δ
Au	2.88	2.83	2.82	2.72	2.69	2.79	2.73	+0.06
Pt		2.77	2.76	2.67	2.63	2.73	2.71	+0.02
Pd			2.75	2.65	2.62	2.72	2.71	+0.01
Cu				2.56	2.52	2.62	2.66	−0.04
Ni					2.49	2.59	2.64	−0.05

Table 8 Calculated interatomic distances d_{Vegard} vs. observed maximum R_{PDFmax} in the total PDF in AuCuNiPd MEA together with their difference $\Delta = d_{Vegard} - R_{PDFmax}$. All values are given in Å

	Au	Pd	Cu	Ni	d_{Vegard} (calculated)	R_{PDFmax} (observed)	Δ
Au	2.88	2.82	2.72	2.69	2.78	2.70	+0.08
Pd		2.75	2.65	2.62	2.71	2.65	+0.06
Cu			2.56	2.52	2.61	2.64	−0.03
Ni				2.49	2.58	2.63	−0.05

One of the important motivations of our work was the validation of correlations between the averaged MSDs (or MSRDs) and the yield strength in the alloys considered. Our results reveal that the averaged MSDs for AuCuNiPdPt HEA and AuCuNiPd MEA are comparable, 0.029 ± 0.005 Å² and 0.03 ± 0.005 Å², respectively, while the average MSRD of HEA is only slightly lower than those for MEA: 0.021 ± 0.004 Å² and 0.023 ± 0.003 Å², respectively. At the same time, AuCuNiPdPt HEA was found to have a significantly higher yield strength of 881 MPa as compared to the yield strength of AuCuNiPd MEA, which is almost twice lower (469 MPa) [23]. Thus, there appears to be no straightforward correlation between the average atomic displacements and the yield strength in Au-Cu-Ni-Pd-Pt based alloys. Besides, considering the asymmetry of the PDFs peaks related to the first coordination shell, the four-component AuCuNiPd MEA seems to be more distorted than the five-component AuCuNiPdPt, which is explicitly evident in the PDFs of Pd (total and partial). This distinction cannot be explained by the differences in shear moduli of these alloys as they are expected to be very similar: 51.2 GPa for AuCuNiPdPt and 48.75 GPa for AuCuNiPd according to Vegard's law. Therefore, the strength behavior of Au-Cu-Ni-Pd-Pt based alloys shows clear signs of being different from that of Cr-Mn-Fe-Co-Ni systems, where a direct correlation between the yield strength normalized by the shear modulus and the square root of the mean square displacement was found [29]. Moreover, if a measure of the elastic interactions between dislocations and the misfit strains in the crystal lattice can still be described by positional disorder expressed as a single average atomic displacement parameter for a whole system, the missing correlation between the averaged MSDs and the yield strength is a clear indication that the solid solution strengthening in Au-Cu-Ni-Pd-Pt alloys is not only represented by elastic interactions. Rather, chemical interactions, such as solute-solute interactions [54, 55] and short-range ordering [56], needed more attention to their detailed studies in the future.

Interestingly, the formal comparison between Au-Cu-Ni-Pd-Pt and known Cr-Mn-Fe-Co-Ni systems suggests the larger averaged MSD and MSRD values for the Cantor alloy: The averaged values for the AuCuNiPdPt found in our work are equal to 0.029 ±

0.005 Å² (MSD) and 0.021 ± 0.003 Å² (MSRD), and both of them are smaller as compared to those in the equiatomic single-phase fcc CrMnFeCoNi where they are equal to 0.038 ± 0.010 Å² (MSD) and 0.030 ± 0.005 Å² (MSRD) [35] (here, the standard deviation is used as the estimation of the uncertainty for the averaged MSD and MSRD values since all types of atoms are considered as equivalent). However, the observed difference is not crucial taking into account the error bars. Note also that the shape of PDFs in AuCuNiPdPt HEA is pronouncedly asymmetric for particular principal components contrary to Cantor alloy where all constituent elements reveal symmetric displacements from their equilibrium lattice positions according to the symmetric shape of their PDFs. Taking into account only the differences in the MSDs and MSRDs of AuCuNiPdPt and CrMnFeCoNi HEAs, one can conclude that the lattice distortions are slightly stronger in CrMnFeCoNi. However, none of the MSD or MSRD parameters takes into account the asymmetry of atom distribution around the regular lattice positions in the AuCuNiPdPt alloy. The asymmetric distribution found for particular types of atoms demonstrates that only particular elements are strongly displaced from their ideal lattice positions. Thus, a single value may not be sufficient to adequately describe the overall distortion of the lattice.

5   Conclusions

Multi-principal components AuCuNiPdPt HEA and AuCuNiPd MEA have been studied in our work with the use of multi-edge EXAFS spectroscopy in combination with RMC simulations. Both alloys have revealed a number of peculiarities in their component-dependent lattice relaxations, highlighting some preferences in the element-specific local environments of principal components at the atomic scale.

The total PDFs, calculated from coordinates of atoms in the RMC simulation boxes related to final atomic configurations after a simultaneous fit to RT EXAFS spectra collected at the absorption edges of each principal component for both alloys, demonstrate the pronounced asymmetry and the shift of their first maxima towards shorter distances for the small size Ni/Cu atoms while the PDFs of larger Au/Pt atoms are much more symmetric and do not show a visible shift. At the same time, the statistically-averaged atomic displacements represented by MSD and MSRD show that smaller Ni/Cu atoms are significantly more displaced from their equilibrium lattice positions as compared to larger Au/Pt atoms. Together with a positive deviation of the experimental lattice parameter from the theoretical ones calculated by Vegard's law, this indicates that in multi-principal component Au-Cu-Ni-Pd-Pt alloys consisting of atoms with large differences in sizes, the larger atoms are more rigid in the crystallographic lattice positions whereas the small atoms are more displaced. In addition, indications of preferential next-neighbour bonding of larger Au atoms with smaller Cu/Ni atoms were found. The comparison of local environments represented by PDFs in the five-component AuCuNiPdPt HEA and four-component AuCuNiPd MEA indicates that Pd atoms are experiencing the largest changes in their nearest-neighbors bonding depending on the composition. The shape of partial PDFs supports these findings.

The fact that both alloys show very similar atomic displacement parameters, despite the yield strengths being almost twice different, can be interpreted as direct evidence that in Au-Cu-Ni-Pd-Pt based alloys the strengthening is not exclusively determined by elastic interactions between the stress–strain field of the dislocations and the lattice. Rather, other contributions such as chemical interactions must be given greater attention in the mechanistic description of solid solution strengthening in the future.

Even if the lack of correlation cannot be solely explained by the asymmetry of the PDFs uncovered in our work, the asymmetry observed for some elements in Au-Cu-Ni-Pd-Pt based alloys raises the question of whether a single displacement parameter is sufficient to adequately describe and compare the lattice distortions in all alloys of interest. In particular, since only symmetric PDFs were observed in previous studies of different forms of the Cantor alloy. Thus, new approaches are necessary to correctly capture not only the absolute values of mean atomic displacements but also the variations in the interatomic distances reflected in the asymmetry of partial distribution functions. This is particularly important because the asymmetry in atom distributions around the anticipated ideal lattice positions is component-dependent and appears to varying degrees depending on the alloy composition.

Data availability

All data needed to support the conclusions in the paper are presented in the manuscript. Additional data related to this paper may be requested from the corresponding author upon request.

Acknowledgements

Declaration of competing interest

The authors declare that they have no known competing financial interests or personal relationships that could have appeared to influence the work reported in this paper.

Author contribution statement

S. D.: Conceptualization, investigation (XRD and EXAFS), writing – original draft, writing – review & editing. A. K.: Formal analysis (EXAFS and RMC), writing – review & editing, visualization, resources. E. W.: Investigation (EXAFS), resources. J. F.: Investigation (XRD), writing – review & editing, resources. A. S.: Conceptualization, investigation (EXAFS), writing – original draft, writing – review & editing, visualization.

Use of AI statement

None.

References

[1] Yeh, J. W. Recent progress in high-entropy alloys. *Ann. Chimie. Sci. Matériaux* **2006**, *31*, 633–648.

[2] Ye, Y. F.; Zhang, Y. H.; He, Q. F.; Zhuang, Y.; Wang, S.; Shi, S. Q.; Hu, A.; Fan, J.; Yang, Y. Atomic-scale distorted lattice in chemically disordered equimolar complex alloys. *Acta Mater.* **2018**, *150*, 182–194.

[3] Sohn, S. S.; Kwiatkowski da Silva, A.; Ikeda, Y.; Körmann, F.; Lu, W. J.; Choi, W. S.; Gault, B.; Ponge, D.; Neugebauer, J.; Raabe, D. Ultrastrong medium-entropy single-phase alloys designed via severe lattice distortion. *Adv. Mater.* **2019**, *31*, 1807142.

[4] George, E. P.; Curtin, W. A.; Tasan, C. C. High entropy alloys: A focused review of mechanical properties and deformation mechanisms. *Acta Mater.* **2020**, *188*, 435–474.

[5] Gorr, B.; Müller, F.; Azim, M.; Christ, H. J.; Müller, T.; Chen, H.; Kauffmann, A.; Heilmaier, M. High-temperature oxidation behavior of refractory high-entropy alloys: Effect of alloy composition. *Oxid. Met.* **2017**, *88*, 339–349.

[6] Cui, Y.; Shen, J. Q.; Manladan, S. M.; Geng, K. P.; Hu, S. S. Wear resistance of FeCoCrNiMnAl$_x$ high-entropy alloy coatings at high temperature. *Appl. Surf. Sci.* **2020**, *512*, 145736.

[7] Jia, Z.; Nomoto, K.; Wang, Q.; Kong, C.; Sun, L. G.; Zhang, L. C.; Liang, S. X.; Lu, J.; Kruzic, J. J. A self-supported high-entropy metallic glass with a nanosponge architecture for efficient hydrogen evolution under alkaline and acidic conditions. *Adv. Funct. Mater.* **2021**, *31*, 2101586.

[8] Yao, R. Q.; Zhou, Y. T.; Shi, H.; Wan, W. B.; Zhang, Q. H.; Gu, L.; Zhu, Y. F.; Wen, Z.; Lang, X. Y.; Jiang, Q. Nanoporous surface high-entropy alloys as highly efficient multisite electrocatalysts for nonacidic hydrogen evolution reaction. *Adv. Funct. Mater.* **2021**, *31*, 2009613.

[9] Jiang, B. B.; Yu, Y.; Cui, J.; Liu, X. X.; Xie, L.; Liao, J. C.; Zhang, Q. H.; Huang, Y.; Ning, S. C.; Jia, B. H. et al. High-entropy-stabilized chalcogenides with high thermoelectric performance. *Science* **2021**, *371*, 830–834.

[10] Wang, X. Y.; Yao, H. H.; Zhang, Z. W.; Li, X. F.; Chen, C.; Yin, L.; Hu, K. N.; Yan, Y. R.; Li, Z.; Yu, B. et al. Enhanced thermoelectric performance in high entropy alloys Sn$_{0.25}$Pb$_{0.25}$Mn$_{0.25}$Ge$_{0.25}$Te. *ACS Appl. Mater. Interfaces* **2021**, *13*, 18638–18647.

[11] Yang, T. N.; Lu, C. Y.; Velisa, G.; Jin, K.; Xiu, P.; Zhang, Y. W.; Bei, H. B.; Wang, L. M. Influence of irradiation temperature on void swelling in NiCoFeCrMn and NiCoFeCrPd. *Scr. Mater.* **2019**, *158*, 57–61.

[12] Wang, P. W.; Li, M. F.; Malomo, B.; Yang, L. Lattice distortion and re-distortion affecting irradiation tolerance in high entropy alloys. *Nanoscale* **2023**, *15*, 16447–16457.

[13] Pickering, E. J.; Carruthers, A. W.; Barron, P. J.; Middleburgh, S. C.; Armstrong, D. E. J.; Gandy, A. S. High-entropy alloys for advanced nuclear applications. *Entropy* **2021**, *23*, 98.

[14] Chen, B.; Li, S. Z.; Ding, J.; Ding, X. D.; Sun, J.; Ma, E. Correlating dislocation mobility with local lattice distortion in refractory multi-principal element alloys. *Scr. Mater.* **2023**, *222*, 115048.

[15] Yang, D. D.; Chen, B.; Li, S. Z.; Ding, X. D.; Sun, J. Effect of local lattice distortion on the core structure of edge dislocation in NbMoTaW multi-principal element alloys and the subsystems. *Mater. Sci. Eng.: A* **2022**, *855*, 143869.

[16] Fang, Q. H.; Lu, W. Z.; Chen, Y.; Feng, H.; Liaw, P. K.; Li, J. Hierarchical multiscale crystal plasticity framework for plasticity and strain hardening of multi-principal element alloys. *J. Mech. Phys. Solids* **2022**, *169*, 105067.

[17] Nutor, R. K.; Cao, Q. P.; Wang, X. D.; Zhang, D. X.; Fang, Y. Z.; Zhang, Y.; Jiang, J. Z. Phase selection, lattice distortions, and

[18] Simon, A. Intermetallic compounds and the use of atomic radii in their description. *Angew. Chem., Int. Ed.* **1983**, *22*, 95–113.

[19] Miracle, D. B.; Senkov, O. N. A critical review of high entropy alloys and related concepts. *Acta Mater.* **2017**, *122*, 448–511.

[20] Varvenne, C.; Luque, A.; Curtin, W. A. Theory of strengthening in fcc high entropy alloys. *Acta Mater.* **2016**, *118*, 164–176.

[21] Freudenberger, J.; Rafaja, D.; Geissler, D.; Giebeler, L.; Ullrich, C.; Kauffmann, A.; Heilmaier, M.; Nielsch, K. Face centred cubic multi-component equiatomic solid solutions in the Au-Cu-Ni-Pd-Pt system. *Metals* **2017**, *7*, 135.

[22] Thiel, F.; Utt, D.; Kauffmann, A.; Nielsch, K.; Albe, K.; Heilmaier, M.; Freudenberger, J. Breakdown of varvenne scaling in (AuNiPdPt)$_{1-x}$Cu$_x$ high-entropy alloys. *Scr. Mater.* **2020**, *181*, 15–18.

[23] Freudenberger, J.; Thiel, F.; Utt, D.; Albe, K.; Kauffmann, A.; Seils, S.; Heilmaier, M. Solid solution strengthening in medium- to high-entropy alloys. *Mater. Sci. Eng.: A* **2022**, *861*, 144271.

[24] Drescher, S.; Seils, S.; Boll, T.; Kauffmann, A.; Heilmaier, M.; Freudenberger, J. Solid solution strengthening in single-phase Au-Cu-Ni-Pd-Pt-based high-entropy alloys. *J. Alloys Compd.* **2024**, *1002*, 175273.

[25] Ice, G.; Sparks, C.; Robertson, J. L.; Epperson, J. E.; Jiang, X. G. Static atomic displacements in crystalline solid solution alloys. *MRS Online Proc. Libr.* **1996**, *437*, 181–186.

[26] Kim, G.; Diao, H. Y.; Lee, C.; Samaei, A. T.; Phan, T.; de Jong, M.; An, K.; Ma, D.; Liaw, P. K.; Chen, W. First-principles and machine learning predictions of elasticity in severely lattice-distorted high-entropy alloys with experimental validation. *Acta Mater.* **2019**, *181*, 124–138.

[27] Nöhring, W. G.; Curtin, W. A. Design using randomness: A new dimension for metallurgy. *Scr. Mater.* **2020**, *187*, 210–215.

[28] Aidhy, D. S. Chemical randomness, lattice distortion and the wide distributions in the atomic level properties in high entropy alloys. *Comput. Mater. Sci.* **2024**, *237*, 112912.

[29] Okamoto, N. L.; Yuge, K.; Tanaka, K.; Inui, H.; George, E. P. Atomic displacement in the CrMnFeCoNi high-entropy alloy—A scaling factor to predict solid solution strengthening. *AIP Adv.* **2016**, *6*, 125008.

[30] Thiel, F.; Geissler, D.; Nielsch, K.; Kauffmann, A.; Seils, S.; Heilmaier, M.; Utt, D.; Albe, K.; Motylenko, M.; Rafaja, D. et al. Origins of strength and plasticity in the precious metal based high-entropy alloy AuCuNiPdPt. *Acta Mater.* **2020**, *185*, 400–411.

[31] Renaud, G.; Motta, N.; Lançon, F.; Belakhovsky, M. Topological short-range disorder in Au$_{1-x}$Ni$_x$ solid solutions: An extended X-ray-absorption fine-structure spectroscopy and computer-simulation study. *Phys. Rev. B* **1988**, *38*, 5944–5964.

[32] Wu, T. B.; Cohen, J. B. Clustering in a Au-Ni alloy above the miscibility gap. *Acta Metall.* **1983**, *31*, 1929–1935.

[33] Lu, K. Q.; Wu, Z. H.; Dong, J.; Chen, X. P.; Fang, Z. Z. The atomic near neighboring structure of Cu$_{1-x}$Au$_x$ solid solution studied with EXAFS. *Jpn. J. Appl. Phys.* **1993**, *32*, 631–633.

[34] Smekhova, A.; Kuzmin, A.; Siemensmeyer, K.; Luo, C.; Chen, K.; Radu, F.; Weschke, E.; Reinholz, U.; Buzanich, A. G.; Yusenko, K. V. Al-driven peculiarities of local coordination and magnetic properties in single-phase Al$_x$-CrFeCoNi high-entropy alloys. *Nano Res.* **2022**, *15*, 4845–4858.

[35] Smekhova, A.; Kuzmin, A.; Siemensmeyer, K.; Abrudan, R.; Reinholz, U.; Buzanich, A. G.; Schneider, M.; Laplanche, G.; Yusenko, K. V. Inner relaxations in equiatomic single-phase high-entropy cantor alloy. *J. Alloys Compd.* **2022**, *920*, 165999.

[36] Smekhova, A.; Kuzmin, A.; Siemensmeyer, K.; Luo, C.; Taylor, J.; Thakur, S.; Radu, F.; Weschke, E.; Buzanich, A. G.; Xiao, B. et al. Local structure and magnetic properties of a nanocrystalline Mn-rich Cantor alloy thin film down to the atomic scale. *Nano Res.* **2023**, *16*, 5626–5639.

[37] Smekhova, A.; Gaertner, D.; Kuzmin, A.; Buzanich, A. G.; Schuck,

G.; Zizak, I.; Wilde, G.; Yusenko, K. V.; Divinski, S. Anomalies in the short-range local environment and atomic diffusion in single crystalline equiatomic CrMnFeCoNi high-entropy alloy. *Nano Res.* **2024**, *17*, 5336–5348.

[38] Schell, N.; King, A.; Beckmann, F.; Fischer, T.; Müller, M.; Schreyer, A. The high energy materials science beamline (HEMS) at PETRA III. *Mater. Sci. Forum* **2013**, *772*, 57–61.

[39] Rietveld, H. M. A profile refinement method for nuclear and magnetic structures. *J. Appl. Crystallogr.* **1969**, *2*, 65–71.

[40] Lutterotti, L.; Matthies, S.; Wenk, H. R. MAUD (Material Analysis Using Diffraction): A user friendly JAVA program for Rietveld texture analysis and more. In *Proceeding of the Twelfth International Conference on Textures of Materials (ICOTOM-12)*; National Research Press: Montreal, 1999, pp 1599.

[41] Welter, E.; Chernikov, R.; Herrmann, M.; Nemausat, R. A beamline for bulk sample X-ray absorption spectroscopy at the high brilliance storage ring PETRA III. *AIP Conf. Proc.* **2019**, *2054*, 040002.

[42] Kuzmin, A.; Chaboy, J. EXAFS and XANES analysis of oxides at the nanoscale. *IUCrJ* **2014**, *1*, 571–589.

[43] Kalinko, A. XAESA [Online]. 2023. https://gitlab.desy.de/aleksandr. kalinko/xaesa (accessed Sep 30, 2023).

[44] Timoshenko, J.; Kuzmin, A.; Purans, J. EXAFS study of hydrogen intercalation into ReO_3 using the evolutionary algorithm. *J. Phys.: Condens. Matter.* **2014**, *26*, 055401.

[45] Timoshenko, J.; Kuzmin, A.; Purans, J. Reverse Monte Carlo modeling of thermal disorder in crystalline materials from EXAFS spectra. *Comput. Phys. Commun.* **2012**, *183*, 1237–1245.

[46] Timoshenko, J.; Kuzmin, A. Wavelet data analysis of EXAFS spectra. *Comput. Phys. Commun.* **2009**, *180*, 920–925.

[47] Ankudinov, A. L.; Ravel, B.; Rehr, J. J.; Conradson, S. D. Real-space multiple-scattering calculation and interpretation of X-ray-absorption near-edge structure. *Phys. Rev. B* **1998**, *58*, 7565–7576.

[48] Rehr, J. J.; Albers, R. C. Theoretical approaches to X-ray absorption fine structure. *Rev. Mod. Phys.* **2000**, *72*, 621–654.

[49] Dalba, G.; Fornasini, P. EXAFS Debye-Waller factor and thermal vibrations of crystals. *J. Synchrotron Radiat.* **1997**, *4*, 243–255.

[50] Wolfram Research. ElementData [Online]. Wolfram Language function. https://reference.wolfram.com/language/ref/ElementData.html (accessed Feb 1, 2024).

[51] Takeuchi, A.; Yubuta, K.; Wada, T. Critically percolated states in high-entropy alloys with exact equi-atomicity. *Mater. Trans.* **2019**, *60*, 330–337.

[52] The Landolt-Börnstein database [Online]. 2023. http://materials. springer.com (accessed Feb 1, 2024).

[53] Oh, H. S.; Odbadrakh, K.; Ikeda, Y.; Mu, S.; Körmann, F.; Sun, C. J.; Ahn, H. S.; Yoon, K. N.; Ma, D. C.; Tasan, C. C. et al. Element-resolved local lattice distortion in complex concentrated alloys: An observable signature of electronic effects. *Acta Mater.* **2021**, *216*, 117135.

[54] Nag, S.; Curtin, W. A. Effect of solute–solute interactions on strengthening of random alloys from dilute to high entropy alloys. *Acta Mater.* **2020**, *200*, 659–673.

[55] Drescher, S.; Seils, S.; Pohl, D.; Rellinghaus, B.; Kauffmann, A.; Heilmaier, M.; Freudenberger, J. Softening by spinodal decomposition in Au-Cu-Ni-Pd-Pt high-entropy alloys. *Mater. Sci. Eng.: A* **2023**, *887*, 145772.

[56] Nag, S.; Curtin, W. A. Solute-strengthening in metal alloys with short-range order. *Acta Mater.* **2024**, *263*, 119472.